

A Variational Physics-Informed Neural Network Framework Using Petrov-Galerkin Method for Solving Singularly Perturbed Boundary Value Problems

Vijay Kumar¹ and Gautam Singh^{1*}

¹Department of Mathematics, National Institute of Technology Tiruchirappalli, Tiruchirappalli, 620015, Tamil Nadu, India.

*Corresponding author(s). E-mail(s): gautam@nitt.edu;
Contributing authors: vijaykumarmathematics@gmail.com;

Abstract

This work proposes a Variational Physics-Informed Neural Network (VPINN) framework that integrates the Petrov-Galerkin formulation with deep neural networks (DNNs) for solving one-dimensional singularly perturbed boundary value problems (BVPs) and parabolic partial differential equations (PDEs) involving one or two small parameters. The method adopts a nonlinear approximation in which the trial space is defined by neural network functions, while the test space is constructed from hat functions. The weak formulation is constructed using localized test functions, with interface penalty terms introduced to enhance numerical stability and accurately capture boundary layers. Dirichlet boundary conditions are imposed via hard constraints, and source terms are computed using automatic differentiation. Numerical experiments on benchmark problems demonstrate the effectiveness of the proposed method, showing significantly improved accuracy in both the L_2 and maximum norms compared to the standard VPINN approach for one-dimensional singularly perturbed differential equations (SPDEs).

Keywords: Variational physics-informed neural network, Singularly perturbed problem, Petrov-Galerkin method, Automatic differentiation.

MSC Classification: 34D15 , 35B25 , 65M12 , 68T07.

1 Introduction

Singular perturbation problems (SPPs) arise in a wide range of scientific and engineering disciplines, including chemical and nuclear engineering [1], control theory [12], fluid flow modeling [13], water pollution studies [20], and fluid dynamics [24]. In SPPs, the presence of small parameters multiplying the highest-order derivatives leads to boundary layer behavior, characterized by sharp variations near the boundaries or within the interior of the domain. This makes solving such problems particularly challenging.

Many numerical techniques have been developed over the years to solve one- and two-parameter second-order singularly perturbed BVPs, particularly using the finite element method (FEM) [3, 16, 23, 25, 27, 29, 31]. Among these, the Discontinuous Galerkin (DG) method introduced by Reed and Hill in 1973 to address neutron transport problems [21] has emerged as a highly flexible and powerful technique for solving various classes of PDEs. To address the challenges posed by singular perturbations, several DG variants have been proposed, such as the Interior Penalty Discontinuous Galerkin (IPDG) method [2], the Symmetric Interior Penalty Galerkin (SIPG) method [8], and the Non-Symmetric Interior Penalty Galerkin (NIPG) method [26]. For further details on the DG method, readers may refer to book [22]. These methods are particularly effective in handling discontinuities and capturing steep solution gradients, making them well-suited for problems exhibiting boundary or interior layers.

In parallel, Deep Neural Networks (DNNs) have emerged as powerful function approximators capable of learning continuous solutions directly from governing equations. This paradigm shift led to the development of Physics-Informed Neural Networks (PINNs), introduced by Raissi et al. [19], where neural networks are trained to satisfy the differential equations and associated boundary or initial conditions by minimizing a physics-informed loss function. As a mesh-free approach, PINNs can naturally accommodate irregular domains and high-dimensional problems, making them appealing for many applications in scientific computing.

The Finite Basis Physics-Informed Neural Network (FB-PINN) framework [17] incorporates finite element methodology by approximating the solution as a sum of finite basis functions. This structure enhances PINN performance, particularly for multiscale problems, and was extended by Raina et al. [18] to handle complex two-parameter convection-dominated systems. In parallel, to address the limitations of standard PINNs in capturing sharp boundary layers in SPPs, Cao et al. [5] introduced the Parameter Asymptotic PINN (PA-PINN) for one-parameter cases. This approach was later generalized by Boro et al. [4] to effectively solve two-parameter convection-dominated problems, demonstrating improved accuracy through the incorporation of asymptotic information.

Moreover, for problems involving non-smooth solutions, several PINN variants based on the variational (weak) formulation have been proposed. These include a Petrov–Galerkin method that employs DNNs as nonlinear trial functions and uses Legendre polynomials or trigonometric functions as test functions [10]. The hp-VPINN framework [11] introduces hp-refinement by decomposing the computational domain and employing projections onto high-order Legendre polynomial spaces. It constructs the trial space using a globally defined neural network, while the test space consists of locally supported piecewise polynomial functions on each subdomain.

Yadav and Ganesan [30] proposed an artificial neural network (ANNs) augmented stabilization strategy for the Streamline Upwind/Petrov–Galerkin FEM to effectively solve SPPs. Chen et al. [7] introduced a Discontinuous Galerkin-induced Neural Network (DGNN). However, to the best of our knowledge, no article has been published on solving SPPs using the VPINN framework with the Petrov-Galerkin method

In this paper, we develop a VPINN with the Petrov-Galerkin framework to solve one-parameter and two-parameter singularly perturbed BVPs, as well as parabolic PDEs involving small perturbation parameters. The method employs a nonlinear approximation by selecting the trial space as the space of neural networks and the test space as the space of hat functions. Dirichlet boundary conditions are imposed via hard constraints, and source terms are computed through automatic differentiation. For time-dependent parabolic problems, temporal discretization is performed using the backward Euler scheme.

The structure of the paper is as follows: Section 2 provides an overview of ANNs, PINNs, VPINNs, and the dataset associated with the problem under study. Section 3 introduces the model problems, the proposed algorithm, and numerical experiments. Finally, Section 4 concludes the paper.

2 Basics of neural network frameworks

2.1 Artificial neural networks (ANNs)

Let $F : \mathbb{R}^m \rightarrow \mathbb{R}^{m_{out}}$ denotes a feed-forward neural network with $s - 1$ hidden layers and n_L neurons in the L -th layer. Usually, the first and last layers are referred to as the input and output layers, respectively, while all intermediate layers are known as hidden layers. When a network has more than one hidden layer, it is commonly referred to as a DNN. ANNs are widely recognized for their capacity to approximate multivariate functions and are often employed as universal function approximators. In a typical fully connected feedforward network, an input $x \in \mathbb{R}^d$ is mapped to an output $u_\theta(x) \in \mathbb{R}$ via a sequence of affine transformations and nonlinear activation functions. For a network with L layers, the forward pass is defined as:

$$u_\theta(x) = \mathcal{N}_L \circ \Phi \circ \mathcal{N}_{L-1} \circ \cdots \circ \Phi \circ \mathcal{N}_1(x),$$

$$\mathcal{N}_k(x) = W_k \Phi(\mathcal{N}_{k-1}(x)) + b_k, \quad \text{for } 2 \leq L \leq s \quad \text{with } \mathcal{N}_0(x) = x,$$

where $W_k \in \mathbb{R}^{N_k \times N_{k-1}}$ and $b_k \in \mathbb{R}^{N_k}$ denote the trainable weight matrix and bias vector corresponding to layer k . The activation function Φ is a nonlinear map, such as ReLU, sigmoid, hyperbolic tangent (tanh), or leaky ReLU. The collection of all trainable parameters is denoted by $\theta = \{W_k, b_k\}_{k=1}^L$.

In traditional supervised learning, the neural network parameters are optimized by minimizing a loss function over a dataset of labeled examples. However, in the context of scientific machine learning where labeled data may be limited an alternative approach is to encode known physical laws directly into the loss function. A Multilayer Perceptron (MLP) is a feedforward neural network that connects every neuron in one layer to all neurons in the next layer.

ANNs have been widely recognized as powerful tools for addressing complex and unresolved challenges in scientific computing, owing to their universal approximation capabilities and the flexibility offered by their hyper-parameter tuning. ANNs have been effectively employed for solving PDEs [14, 28]. Recent studies have also investigated hybrid approaches that integrate ANNs with classical numerical techniques [9]. For instance, one study proposed the Proper orthogonal decomposition neural network (POD-NN) method, where ANNs are utilized during the interpolation stage to develop a non-intrusive Radial Basis (RB) method based on proper orthogonal decomposition. Similarly, [6] introduced a smart FEM that learns a direct mapping between element-level inputs and outputs to alleviate the computational burden of large-scale problems. However, in both approaches, FEM is not directly embedded within the deep learning framework, but rather employed for data generation or as a means of accelerating specific numerical operations. A visualization of an ANNs is provided in Figure 1.

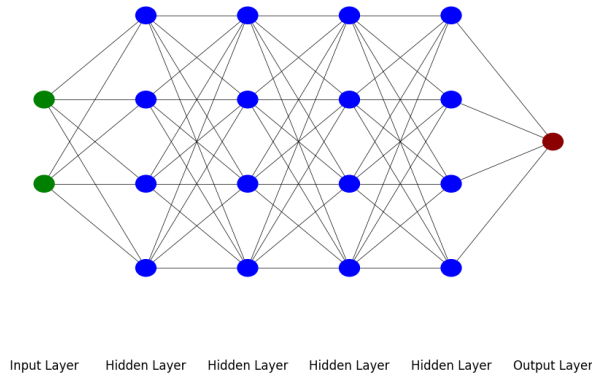


Fig. 1: Visualization of artificial neural network.

2.2 Physics-informed neural networks (PINNs)

PINNs, as introduced in [19], provide a robust approach for addressing both forward and inverse problems involving differential and integro-differential equations. They are particularly effective in scenarios where data is limited, uncertain, or derived from multiple sources of varying fidelity. One of the defining advantages of PINNs is their ability to integrate diverse sources of information such as governing equations, boundary and initial conditions, and empirical observations directly into the model's loss function. This integration constrains the solution space, ensuring that the learned solution adheres to the underlying physical laws. Since PINNs are mesh-free, they recast the task of solving PDEs as an optimization problem over a loss function, rather than relying on traditional discretization techniques. As a result, they can achieve strong generalization with fewer data points compared to conventional purely data-driven neural networks.

Despite their effectiveness, applying PINNs to SPPs remains challenging. This is due to the nature of SPPs, where the solution typically exhibits rapid variations near boundary or interior layers, while varying more smoothly elsewhere. Capturing such multi-scale behavior with a single deep neural network can be difficult. A practical approach in such cases is to divide the computational domain into multiple regions, with each region modeled independently based on its specific characteristics. This strategy can improve the solution’s accuracy and efficiency. Nevertheless, domain decomposition techniques, such as those proposed in [15], often depend on prior knowledge of the layer structure or singularity locations information that is not always available in practical applications.

PINNs incorporate prior knowledge of physical laws such as partial differential equations (PDEs) into the neural network training. Consider a PDE of the form:

$$\mathcal{D}(u(x)) = r(x), \quad x \in I \subset \mathbb{R}^d, \quad \mathcal{B}(u(x)) = 0, \quad x \in \partial I,$$

where \mathcal{D} is a differential operator and \mathcal{B} denotes the boundary conditions. The neural network $u_\theta(x)$ is used to approximate the solution. The residual is defined by:

$$v(x) := \mathcal{D}(u_\theta(x)) - r(x).$$

The total PINN loss function includes two components:

$$\text{Loss}_{\text{PINN}}(\theta) = \frac{1}{N_f} \sum_{i=1}^{N_f} |v(x_i^f)|^2 + \frac{1}{N_u} \sum_{i=1}^{N_u} |u_\theta(x_i^u) - g(x_i^u)|^2,$$

where $\{x_i^f\}_{i=1}^{N_f} \subset I$ are the *interior collocation points* at which the differential equation is enforced, and $\{x_i^u\}_{i=1}^{N_u} \subset \partial I$ are the *boundary points* where the Dirichlet boundary condition $u(x) = g(x)$ is imposed. Here, N_f and N_u denote the total number of interior and boundary points, respectively.

To improve accuracy at the boundary, one may enforce hard constraints by modifying the neural network architecture so that the boundary conditions are exactly satisfied, i.e., by constructing $u_\theta(x)$ such that $u_\theta|_{\partial I} = g(x)$. This eliminates the need to include a penalty term for boundary conditions in the loss and can improve convergence and accuracy.

2.3 Variational physics-informed neural networks (VPINNs)

VPINNs extend the PINN framework by enforcing the residual in a variational or weak form. Instead of minimizing $u(x)$ pointwise, VPINNs require that the residual be orthogonal to a set of test functions $\{v_j(x)\}_{j=1}^M$, leading to:

$$\int_I u(x) v_j(x) dx = 0 \quad \forall j = 1, \dots, M,$$

that is,

$$\int_I (\mathcal{D}(u_\theta(x)) - r(x)) v_j(x) dx = 0.$$

The corresponding VPINN loss function is:

$$\text{Loss}_{\text{VPINN}}(\theta) = \sum_{j=1}^M \left| \int_I (\mathcal{D}(u_\theta(x)) - r(x)) v_j(x) dx \right|^2 + \text{MSE}_u.$$

As in PINNs, the boundary loss term is:

$$\text{MSE}_u = \frac{1}{N_u} \sum_{i=1}^{N_u} |u_\theta(x_i^u) - g(x_i^u)|^2.$$

Alternatively, using hard constraint boundary conditions can be implemented in VPINNs as well by ensuring the network structure satisfies $u_\theta(x) = g(x)$ on ∂I exactly.

The test functions v_j are typically selected from a piecewise polynomial basis, such as linear hat functions or higher-order finite element bases. All integrals are evaluated using suitable numerical quadrature schemes.

2.4 Dataset

This subsection focuses on data generated from one-dimensional singularly perturbed differential equations. In contrast to other methods, our VPINN framework employs 36 test functions and 1000 quadrature points. A hard boundary constraint is applied to enforce Dirichlet conditions. For every neural network architecture featuring 4 hidden layers with 20 neurons each and the tanh activation function. For the convection-diffusion problem, the model is trained using the Adam optimizer with a learning rate of 10^{-3} and is then fine-tuned using the L-BFGS optimizer for 1500 epochs. In contrast, for the reaction-diffusion and two-parameter singularly perturbed problems, only the L-BFGS optimizer is used for 1500 epochs.

For time-dependent problems, the framework employs 18 test functions and incorporates 100 quadrature points in both space and time. Training begins with the Adam optimizer employing a learning rate of 10^{-3} and is then fine-tuned using the L-BFGS optimizer for 1000 epochs, while maintaining the same network architecture and dataset structure as in the static case.

3 Model problems and numerical experiments

3.1 The convection-diffusion BVPs

We examine the following one-parameter singularly perturbed BVPs:

$$\begin{cases} -\epsilon u''(x) + b(x)u'(x) + c(x)u(x) = r(x), & x \in I = (0, 1), \\ u(0) = u(1) = 0. \end{cases} \quad (1)$$

Here, $0 < \epsilon \ll 1$ is a small parameter, and the function $b(x), c(x)$ and $r(x)$ are sufficiently smooth and satisfy the conditions $b(x) \geq \alpha > 0$, $c(x) - \frac{b'(x)}{2} > 0$, $\forall x \in I$, for constant α . Therefore, the solution $u(x)$ of (1) features a boundary layer at $x = 1$.

The finite element formulation of the BVPs (1) seeks a function $u \in H_0^1(I)$ such that, $\forall v \in H_0^1(I)$,

$$a(u, v) = (r, v), \quad (2)$$

where the bilinear form $a(\cdot, \cdot)$ is given by

$$a(u, v) = \int_I \epsilon u'(x) v'(x) dx + \int_I b(x) u'(x) v(x) dx + \int_I c(x) u(x) v(x) dx,$$

and the linear functional on the right-hand side is defined as

$$(r, v) = \int_I r(x) v(x) dx.$$

We denote by I_h a mesh that subdivides the domain I into a finite number of elements. Corresponding to this mesh, we define a finite-dimensional subspace $V_h \subset H_0^1(I)$. We also define the neural network-based trial space as $U_{NN} = \{u_\theta(x) = \text{DNN}(x; \theta) \mid \theta \in \Theta\}$, where $\text{DNN}(x; \theta)$ denotes a deep neural network formed by sequential layers of linear mappings combined with nonlinear activation functions, and Θ represents the collection of all trainable parameters.

The discrete variational problem associated with equation (2) is then stated as follows:

Find $u_h \in U_{NN}$ such that, $\forall v \in V_h$,

$$a_h(u_h, v) = (r, v),$$

where the notation $a_h(\cdot, \cdot)$ implies that integration is performed element-wise over the partition I_h .

The VPINN algorithm for one-parameter convection-diffusion problem is illustrated in Algorithm 1. Figure 2 provides a visual representation of the Algorithm 1.

Example 1. Consider the problem in (1) with $b(x) = -(1+x)$ and $c(x) = 1$, where the source function $r(x)$ is computed from the exact solution

$$u(x) = 1 - x - e^{-x/\epsilon} + x e^{-x/\epsilon}.$$

We executed the code for 1500 iterations and the Maximum error, Relative maximum error, L_2 error, Relative L_2 error and Loss at 1500 epoch obtained are presented in Table 1. Figure 3 presents a comparison between the exact solution and VPINN approximation for different parameter values. Figure 4 illustrates the absolute error plots for the same example, while Figure 5 shows the loss versus epoch curves, corresponding to the final iteration of our algorithm.

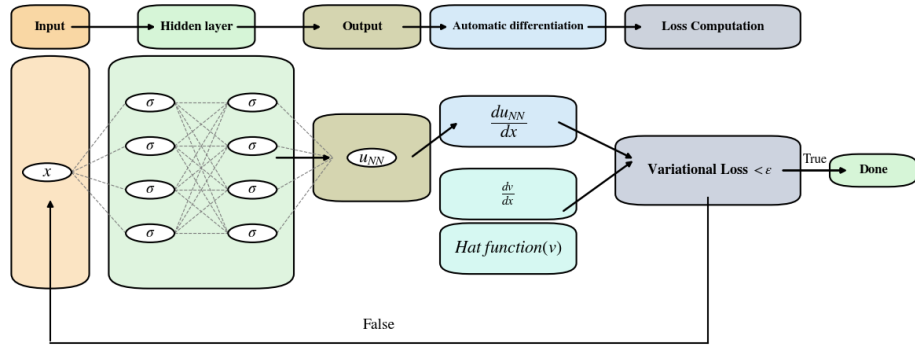


Fig. 2: VPINN algorithm flowchart.

Table 1: Loss and Error for Example 1.

ϵ	Loss	maximum	Rel-maximum	L_2	Rel- L_2
10^{-1}	4.64323e-08	3.74317e-05	5.39757e-05	2.11394e-05	4.58645e-06
10^{-2}	3.82179e-07	2.89887e-04	3.07275e-04	1.43689e-04	2.55847e-05
10^{-3}	4.27739e-06	5.31852e-04	5.37301e-04	1.45876e-04	2.55877e-05
10^{-4}	1.64225e-05	1.77413e-03	1.79224e-03	9.12843e-04	1.60119e-04
10^{-5}	1.80347e-05	2.38985e-03	2.41423e-03	1.16507e-03	2.04361e-04

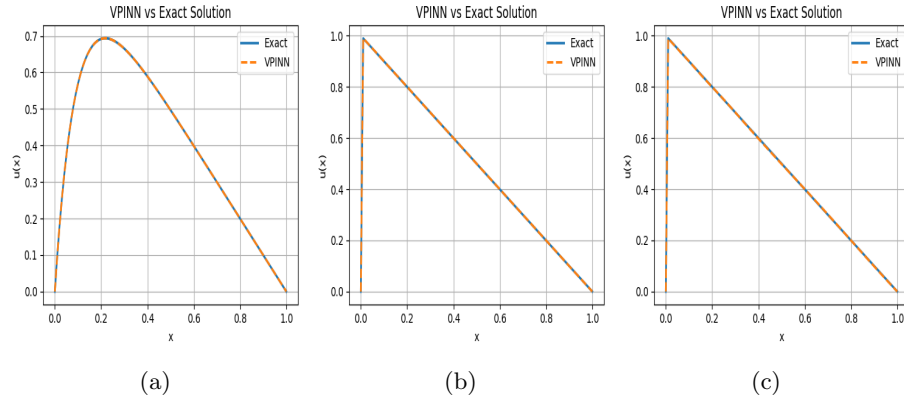


Fig. 3: Comparison between Exact and VPINN solution for Example 1 with different value of perturbation parameter $\epsilon = 10^{-1}, 10^{-3}$, and 10^{-5} , corresponding to subfigures (a), (b), and (c), respectively.

Algorithm 1 VPINN Algorithm for Solving $-\epsilon u''(x) + b(x)u'(x) + c(x)u(x) = r(x)$ in $(0, 1)$ with $u(0) = u(1) = 0$

- 1: **Input:** Small parameter $\epsilon > 0$, number of collocation points N , number of test functions M
- 2: **Define:** Trial function $\mathcal{T}_\theta(x) := x(1-x) \cdot \text{NN}_\theta(x)$ to satisfy boundary conditions
- 3: **Generate:** Uniformly spaced collocation points $\{x_j\}_{j=1}^N \subset (0, 1)$
- 4: **Construct:** Piecewise linear hat test functions $\{v_i(x)\}_{i=1}^M$ on a mesh $\{x_k\}_{k=0}^{M+1}$
- 5: **Compute:** Exact solution $u_{\text{exact}}(x)$ and source term $r(x) = -\epsilon u''_{\text{exact}}(x) + b(x)u'_{\text{exact}}(x) + c(x)u_{\text{exact}}(x)$ using automatic differentiation
- 6: **for** $i = 1$ to M **do**
- 7: Define weak residual for each test function $v_i(x)$:

$$R_i(\theta) := \int_0^1 (-\epsilon^2 \mathcal{T}_\theta''(x) + b(x)\mathcal{T}_\theta'(x) + c(x)\mathcal{T}_\theta(x) - r(x)) v_i(x) dx$$

- 8: **end for**
- 9: **Define:** VPINN loss function as:

$$\mathcal{L}(\theta) := \frac{1}{M} \sum_{i=1}^M (R_i(\theta))^2$$

- 10: **Initialize:** Neural network weights θ randomly
 - 11: **Train:** Minimize $\mathcal{L}(\theta)$ first using Adam and then fine-tuned using the L-BFGS optimizer with closure-based backpropagation
 - 12: **Return:** Trained network $\mathcal{T}_\theta(x)$ approximating the solution $u(x)$
-

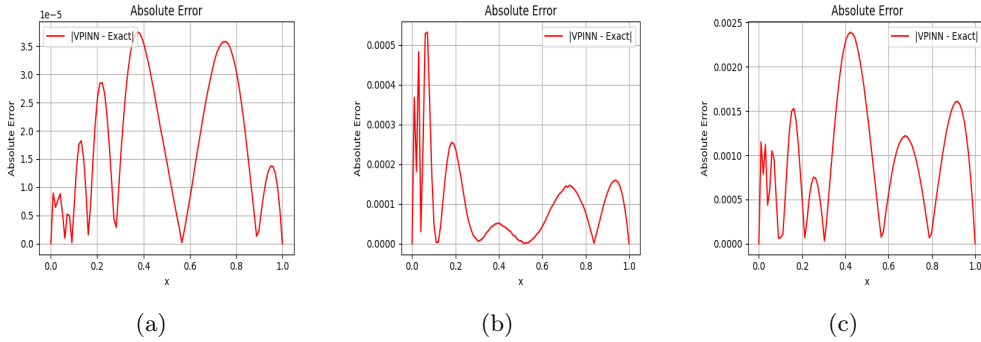


Fig. 4: Error vs x for Example 1 with different value of perturbation parameter $\epsilon = 10^{-1}, 10^{-3}$, and 10^{-5} , corresponding to subfigures (a), (b), and (c), respectively.

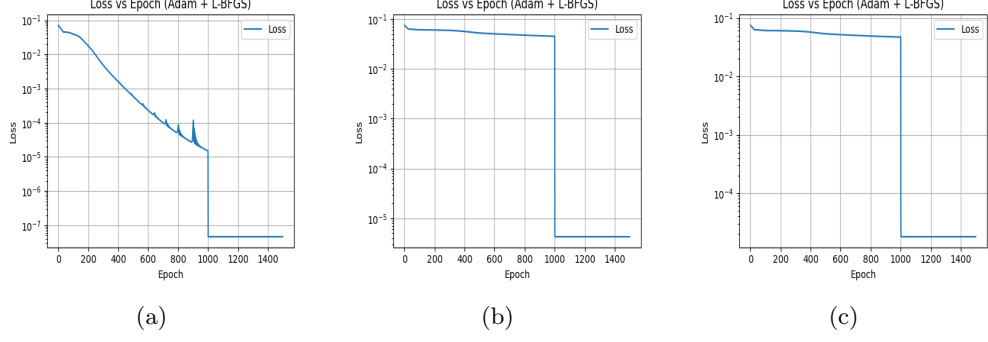


Fig. 5: Loss vs Epoch for Example 1 with different value of perturbation parameter $\epsilon = 10^{-1}, 10^{-3}, 10^{-5}$, corresponding to subfigures (a), (b), and (c), respectively.

3.2 Initial boundary-value problem (IBVP)

Consider the following singularly perturbed parabolic PDEs with one-parameters in the domain $G = I \times (0, T]$, where $I = (0, 1)$:

$$\begin{cases} u_t - \epsilon u_{xx} + b(x)u_x + c(x)u(x, t) = r(x, t), & x \in I = (0, 1), \\ u(0, t) = u(1, t) = 0, & 0 \leq t \leq T, \\ u(x, 0) - \phi(x) = 0, & \text{for } x \in [0, 1], \end{cases} \quad (3)$$

Here, $0 < \epsilon \ll 1$ is a small parameter, and the function $b(x), c(x)$ and $r(x, t)$ are sufficiently smooth and satisfy the conditions $b(x) \geq \alpha > 0$, $c(x) - \frac{b'(x)}{2} > 0$, $\forall x \in I$, for constant α . Therefore solution $u(x, t)$ of (3) exhibits boundary layers of at $x = 1$.

The finite element formulation of the BVPs (3) is given by. Find $u \in H_0^1(I)$, such that $\forall v \in H_0^1(I)$

$$a(u, v) = (r, v), \quad (4)$$

where the bilinear form $a(., .)$ is defined by

$$\int_I \frac{\partial u}{\partial t} v dx + \int_I \epsilon \frac{\partial u}{\partial x} \frac{\partial v}{\partial x} dx + \int_I b(x) \frac{\partial u}{\partial x} v dx + \int_I c(x) u v dx = \int_I r(x) v dx,$$

At each time step $t = t_m$ ($1 \leq m \leq M$), we have the following

$$a(u^m, v) = (r^m, v), \quad (5)$$

$$\begin{aligned} \int_I \frac{\partial u^m}{\partial t} v dx + \int_I \epsilon \frac{\partial u^m}{\partial x} \frac{\partial v}{\partial x} dx + \int_I b(x) \frac{\partial u^m}{\partial x} v dx + \int_I c(x) u^m v dx &= \int_I r^m v dx, \\ \int_I \frac{(u^m - u^{m-1})}{\Delta t} v dx + \int_I \epsilon \frac{\partial u^m}{\partial x} \frac{\partial v}{\partial x} dx + \int_I b(x) \frac{\partial u^m}{\partial x} v dx + \int_I c(x) u^m v dx &= \int_I r^m v dx, \\ b(u^m, v) &= (g^m, v) \end{aligned}$$

$$b(u^m, v) = \int_I \epsilon \frac{\partial u^m}{\partial x} \frac{\partial v}{\partial x} dx + \int_I b(x) \frac{\partial u^m}{\partial x} v dx + \int_I \left(c(x) + \frac{1}{\Delta t} \right) u^m v dx$$

$$(g^m, v) = \int_I \left(r^m + \frac{u^{m-1}}{\Delta t} \right) v(x) dx.$$

We denote by I_h a mesh that subdivides the domain I into a finite number of elements. The discrete variational problem associated with equation (5) is stated as follows:

Find $u_h \in U_{NN}$ such that, $\forall v \in V_h$,

$$b_h(u_h^m, v) = (g^m, v).$$

where the notation $b_h(\cdot, \cdot)$ implies that integration is performed element-wise over the partition I_h .

The VPINN algorithm for Parabolic convection-diffusion IBVP is illustrated in Algorithm 2.

Example 2. Consider the parabolic one-parameter IBVP (3) with $b(x) = 1$ and $c(x) = 1$. The source term $r(x, t)$ and initial condition $\phi(x)$ are chosen from the exact solution

$$u(x, t) = e^{-t} (1 - e^{-(1-x)/\epsilon}) \sin x.$$

We executed the code for 1000 iterations, and the computed errors at the final time $T = 1$ are reported in Table 2. Figure 6 illustrates the comparison between the exact solution and the VPINN approximation for various parameter values at $T = 1$. The corresponding absolute error distributions are shown in Figure 7. Figure 8 displays the loss versus epoch curves, which represent the convergence behavior during the final iteration of the algorithm. Additionally, Figure 9 provides a surface plot comparison between the exact solution and the VPINN approximation for various values of the perturbation parameter.

Table 2: Loss and Error for Example 2 at the final time $T = 1$.

ϵ	Loss	maximum	Rel-maximum	L_2	Rel- L_2
10^{-1}	3.79781e-07	4.73222e-04	2.05343e-03	2.63204e-04	1.68000e-03
10^{-2}	8.91816e-06	4.82719e-03	1.62415e-02	1.33777e-03	7.13798e-03
10^{-3}	3.38240e-06	2.65777e-03	8.64250e-03	1.30504e-03	6.87290e-03
10^{-4}	1.31400e-04	8.27751e-03	2.69155e-02	2.06461e-03	1.08731e-02
10^{-5}	3.39702e-05	2.12925e-02	6.92356e-02	2.31294e-03	1.21809e-02

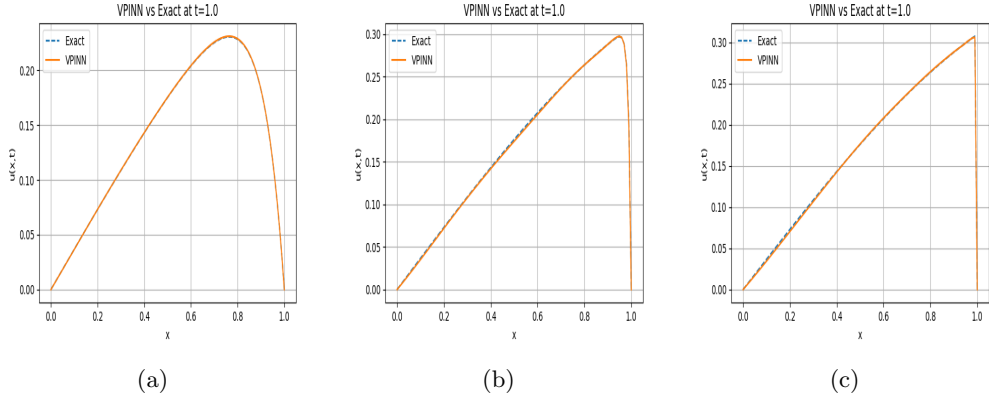


Fig. 6: Comparison between Exact and VPINN solution for Example 2 with different value of perturbation parameter $\epsilon = 10^{-1}, 10^{-2}$, and 10^{-3} , corresponding to subfigures (a), (b), and (c), respectively.

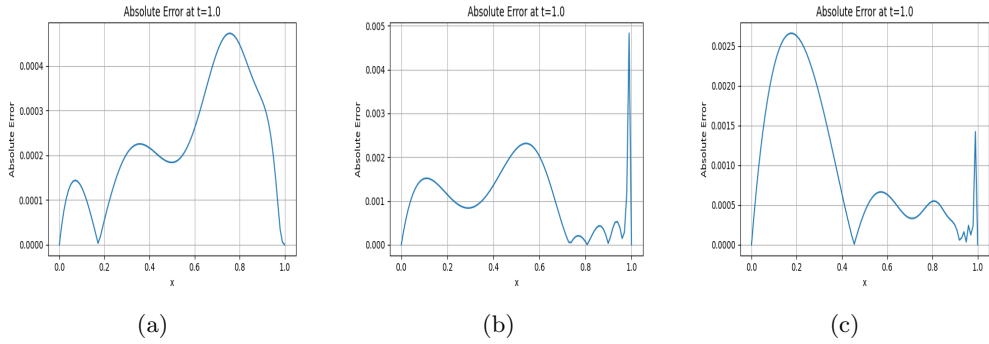


Fig. 7: Error vs x for Example 2 with different value of perturbation parameter $\epsilon = 10^{-1}, 10^{-2}$, and 10^{-3} , corresponding to subfigures (a), (b), and (c), respectively.

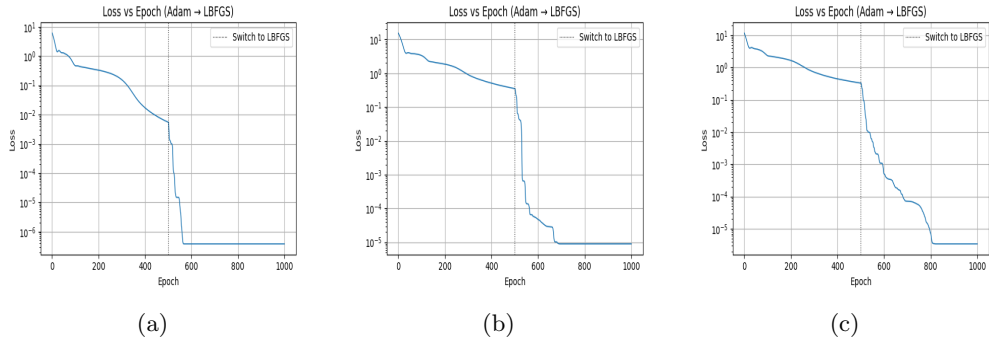


Fig. 8: Loss vs Epoch for Example 2 with different value of perturbation parameter $\epsilon = 10^{-1}, 10^{-2}$, and 10^{-3} , corresponding to subfigures (a), (b), and (c), respectively.

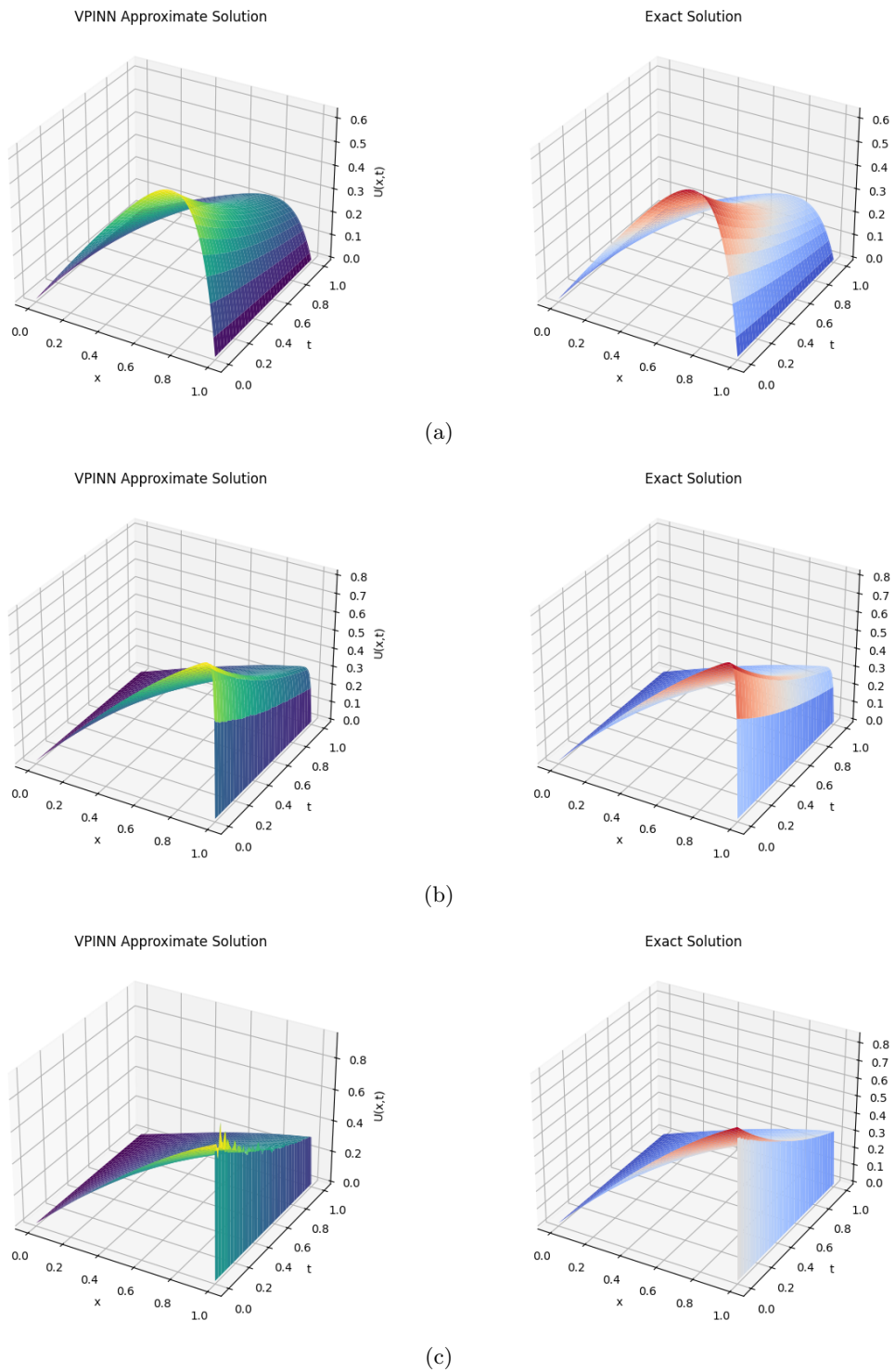


Fig. 9: Comparison between exact solution vs approximate solution for Example 2 with different value of perturbation parameter $\epsilon = 10^{-1}, 10^{-2},$ and 10^{-3} , corresponding to subfigures (a), (b), and (c), respectively.

Algorithm 2 VPINN for Solving $u_t - \varepsilon u_{xx} + b(x)u_x + c(x)u = r(x, t)$ with Dirichlet Boundary Conditions

- 1: **Given:** PDE $u_t - \varepsilon u_{xx} + b(x)u_x + c(x)u = r(x, t)$ on $(x, t) \in (0, 1) \times (0, 1]$
- 2: **Inputs:** Diffusion parameter $\varepsilon > 0$, spatial nodes N_x , time steps N_t , test functions M
- 3: Discretize: $x_i \in [0, 1]$, $t_n = n\Delta t$, with $\Delta t = \frac{1}{N_t}$
- 4: Initialize solution $u^0(x) = u_{\text{exact}}(x, 0)$
- 5: **for** $n = 1$ to N_t **do**
- 6: Define neural network trial solution $u_\theta(x) = x(1 - x) \cdot \text{NN}(x)$ to boundary condition.
- 7: Compute source term $r(x, t_n)$ using autograd from $u_{\text{exact}}(x, t)$
- 8: Construct residual:

$$R(x) = \frac{u_\theta(x) - u^{n-1}(x)}{\Delta t} - \varepsilon u_{\theta,xx} + b(x)u_{\theta,x} + c(x)u_\theta(x) - r(x, t_n)$$

- 9: Define weak loss using hat test functions $\{\phi_i(x)\}_{i=1}^M$:

$$\mathcal{L}(\theta) = \frac{1}{M} \sum_{i=1}^M \int_0^1 R(x)\phi_i(x) dx \approx \frac{1}{M} \sum_{i=1}^M \text{MSE}(R(x)\phi_i(x))$$

Mean Squared Error (MSE):

$$\text{MSE}(g(x)) = \frac{1}{N_x} \sum_{j=1}^{N_x} (g(x_j))^2$$

- 10: Train the neural network by minimizing $\mathcal{L}(\theta)$ first using Adam and then fine-tuned using the L-BFGS optimizer
 - 11: Set $u^n(x) \leftarrow u_\theta(x)$
 - 12: **end for**
 - 13: **Return:** VPINN predictions $u_\theta(x, t_n)$ for $n = 1, \dots, N_t$
 - 14: **Postprocess:** Compute relative L^2 and L^∞ errors, visualize solution surfaces
-

3.3 The reaction-diffusion BVP

We examine the following one-parameter singularly perturbed BVPs:

$$\begin{cases} -\varepsilon^2 u''(x) + c(x)u(x) = r(x), & x \in I = (0, 1), \\ u(0) = u(1) = 0. \end{cases} \quad (6)$$

Here, $0 < \varepsilon \ll 1$ is a small parameter, and the function $c(x)$ and $r(x)$ are sufficiently smooth and satisfy the conditions $c(x) \geq \beta^2 > 0$, $\forall x \in I$, for constant β . Therefore solution $u(x)$ of (6) exhibits boundary layers at $x = 0$ and $x = 1$.

The finite element formulation and algorithm will be similar to the model problem (1).

Example 3. Consider the problem in (6) with $c(x) = 1$, where the source function $r(x)$ is computed from the exact solution

$$u(x) = (1 + \exp(-1/\epsilon) - \exp(-x/\epsilon) - \exp(-(1-x)/\epsilon)).$$

We executed the code for 1500 iterations and the Maximum error, Relative maximum error, L_2 error, Relative L_2 error and Loss at 1500 epoch obtained are presented in Table 3. Figure 10 presents a comparison between the exact and VPINN solutions for different parameter values. Figure 11 illustrates the absolute error plots for the same example, while Figure 12 shows the loss versus epoch curves, corresponding to the final iteration of our algorithm.

Table 3: Loss and Error for Example 3.

ϵ	Loss	maximum	Rel-maximum	L_2	Rel- L_2
10^{-1}	2.97115e-08	4.52220e-04	4.58385e-04	2.16551e-04	2.60098e-05
10^{-2}	1.66846e-06	4.05634e-02	4.05634e-02	7.09868e-03	7.24451e-04
10^{-3}	2.29249e-06	2.59871e-02	2.59871e-02	4.08781e-03	4.12932e-04
10^{-4}	5.23947e-06	3.31051e-02	3.31051e-02	6.11351e-03	6.17558e-04
10^{-5}	2.53564e-06	2.41746e-02	2.41746e-02	6.53846e-03	6.60484e-04

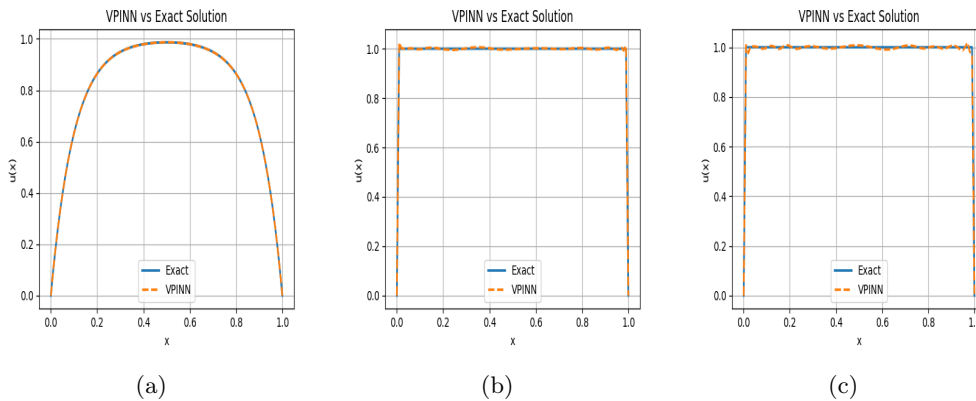


Fig. 10: Comparison between Exact and VPINN solution for Example 3 with different value of perturbation parameter $\epsilon = 10^{-1}, 10^{-3}$, and 10^{-5} , corresponding to subfigures (a), (b), and (c), respectively.

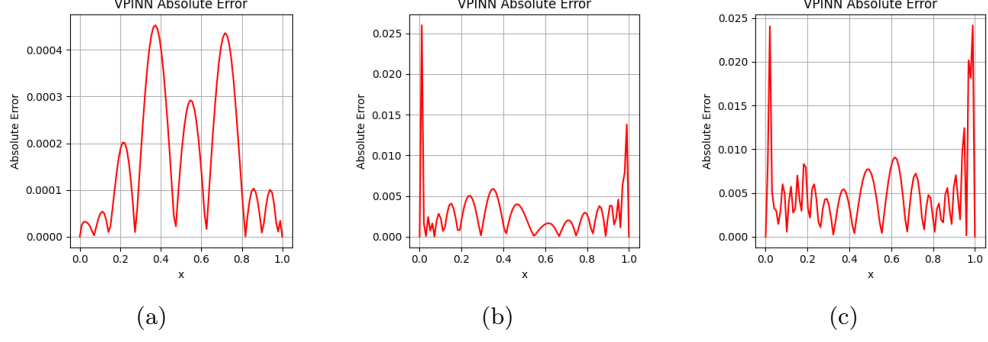


Fig. 11: Error vs x for Example 3 with different value of perturbation parameter $\epsilon = 10^{-1}, 10^{-3},$ and 10^{-5} , corresponding to subfigures (a), (b), and (c), respectively.

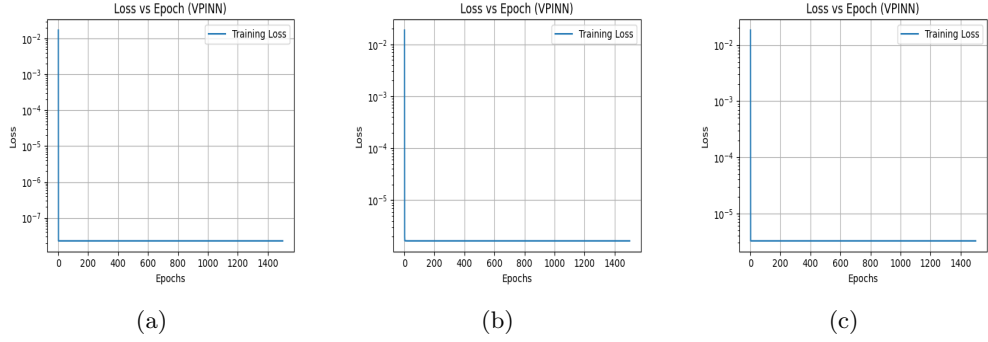


Fig. 12: Loss vs Epoch for Example 3 with different value of perturbation parameter $\epsilon = 10^{-1}, 10^{-3},$ and 10^{-5} , corresponding to subfigures (a), (b), and (c), respectively.

3.4 Two-parameter SPPs

We examine the following two-parameter singularly perturbed BVPs:

$$\begin{cases} -\epsilon u''(x) + \mu b(x)u'(x) + c(x)u(x) = r(x), & x \in I = (0, 1), \\ u(0) = u(1) = 0. \end{cases} \quad (7)$$

Here, $0 < \epsilon \ll 1$ and $0 < \mu \ll 1$ are small perturbation parameter, and the function $b(x), c(x)$ and $r(x)$ are sufficiently smooth and satisfy the conditions $b(x) \geq \alpha > 0$, $c(x) - \frac{\mu b'(x)}{2} > 0, \forall x \in I$, for constant α . Therefore solution $u(x)$ of (7) exhibits boundary layers both the ends of domain i.e, at $x = 0$ and $x = 1$.

Lemma 1. Let z_0 and z_1 be the solution of the characteristic equation.

$$-\epsilon z^2(x) + \mu b(x)z(x) + c(x) = 0.$$

Here, $z_0(x) < 0$, $z_1(x) > 0$ the boundary layers at $x = 0$ and $x = 1$, respectively.

$$\lambda_0 = -\max_{x \in [0,1]} z_0(x), \quad \lambda_1 = \min_{x \in [0,1]} z_1(x),$$

$$\lambda_0 = \max_{x \in [0,1]} \frac{-\mu b(x) + \sqrt{\mu^2 b^2(x) + 4\epsilon c(x)}}{2\epsilon},$$

$$\lambda_1 = \min_{x \in [0,1]} \frac{\mu b(x) + \sqrt{\mu^2 b^2(x) + 4\epsilon c(x)}}{2\epsilon}.$$

Depending on the relationship between ϵ and μ , we can classify (7) into the three regimes:

- If $\epsilon \ll \mu = 1$, then $\lambda_0 = O(1)$ and $\lambda_1 = O(1/\epsilon)$. In this case is similar to convection-diffusion type.
- If $\epsilon \ll \mu^2 \ll 1$, then $\lambda_0 = O(\mu^{-1})$ and $\lambda_1 = O(\mu\epsilon^{-1})$. In this case is similar to diffusion-convection-reaction type.
- If $\mu^2 \ll \epsilon \ll 1$, then $\lambda_0 = O(\mu^{-1/2})$ and $\lambda_1 = O(\epsilon^{-1/2})$. In this case is similar to reaction-diffusion type.

Example 4. Consider the problem in (7) with $b(x) = 1$ and $c(x) = 1$. The source function $r(x)$ is chosen from the exact solution

$$u(x) = \frac{1}{E} \left[\frac{e^{m_1} (e^{1-m_1} - 1) e^{-m_2 x} - (e^{1-m_2} - 1) e^{m_1(1-x)}}{D} - e^{1-x} \right],$$

where $m_{1,2} = \frac{\mu \mp \sqrt{\mu^2 + 4\epsilon}}{2\epsilon}$, $D = 1 - \exp\left(\frac{-\sqrt{\mu^2 + 4\epsilon}}{\epsilon}\right)$, $E = \epsilon - \mu - 1$.

We executed the code for 1500 iterations and the Maximum error, Relative maximum error, L_2 error, Relative L_2 error and Loss at 1500 epoch obtained are presented in Table 4. Figure 13 presents a comparison between the exact and VPINN solutions for different parameter values. Figure 14 illustrates the absolute error plots for the same example, while Figure 15 shows the loss versus epoch curves, corresponding to the final iteration of our algorithm.

Table 4: Loss and Error for Example 4.

ϵ, μ	Loss	maximum	Rel-maximum	L_2	Rel- L_2
$10^{-1}, 10^{-2}$	3.06321e-07	3.80754e-04	3.66852e-04	2.03801e-04	8.37204e-06
$10^{-2}, 10^{-3}$	2.61157e-08	2.89321e-04	1.51199e-04	1.27626e-04	2.79353e-06
$10^{-3}, 10^{-4}$	5.32722e-07	2.85333e-03	1.21211e-03	8.97248e-04	5.37536e-04
$10^{-4}, 10^{-5}$	9.44896e-07	2.15509e-02	8.39448e-03	4.27543e-03	2.45244e-03

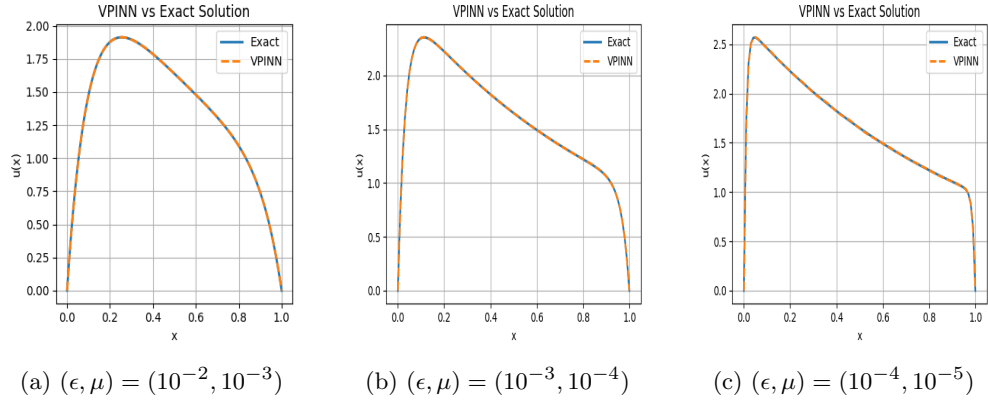


Fig. 13: Comparison between Exact and VPINN solution for Example 4 with different value of perturbation parameter.

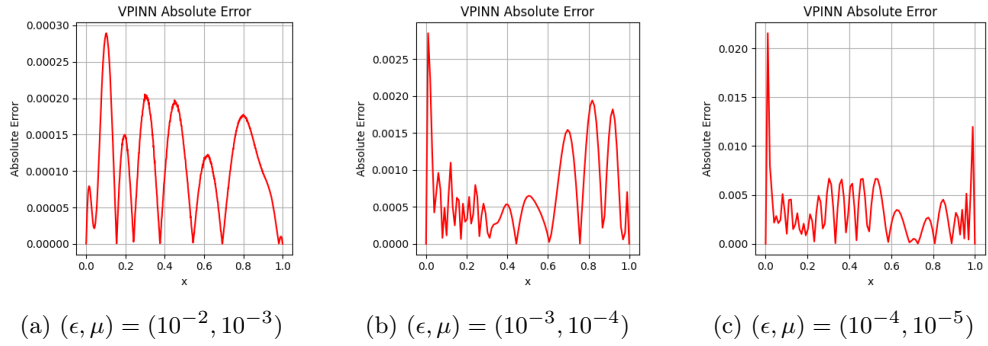


Fig. 14: Error vs x for Example 4 with different value of perturbation parameter.

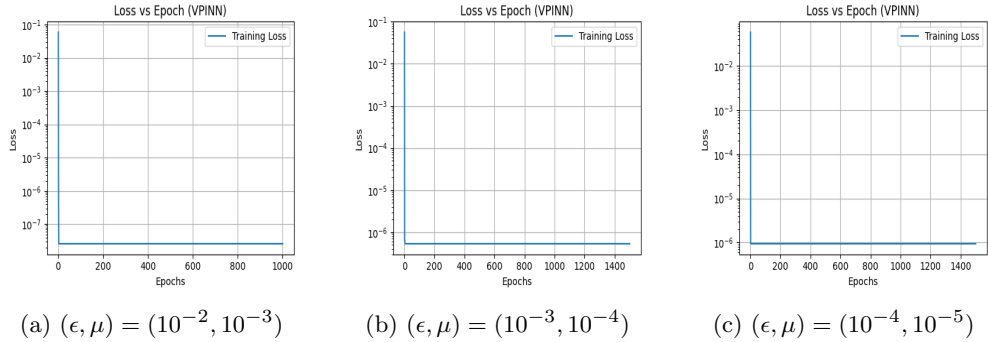


Fig. 15: Loss vs Epoch for Example 4 with different value of perturbation parameter.

3.5 Parabolic two-parameter IBVP

Consider the following singularly perturbed parabolic PDEs with two-parameters in the domain $G = I \times (0, T]$, where $I = (0, 1)$:

$$\begin{cases} u_t - \epsilon u_{xx} + \mu b(x)u_x + c(x)u(x, t) = r(x, t), & x \in I = (0, 1), \\ u(0, t) = u(1, t) = 0, & 0 \leq t \leq T, \\ u(x, 0) - \phi(x) = 0, & \text{for } x \in [0, 1]. \end{cases} \quad (8)$$

Here, $0 < \epsilon \ll 1$ and $0 < \mu \ll 1$ are small perturbation parameter, and the function $b(x), c(x)$ and $r(x, t)$ are sufficiently smooth and satisfy the conditions $b(x) \geq \alpha > 0$, $c(x) - \frac{\mu b'(x)}{2} > 0$, $\forall x \in I$, for constant α . Therefore solution $u(x, t)$ of (8) exhibits boundary layers of both the ends of domain i.e, at $x = 0$ and $x = 1$.

Example 5. Consider the parabolic two-parameter IBVP (8) with $b(x) = 1$ and $c(x) = 1$. The source term $r(x, t)$ and initial condition $\phi(x)$ are chosen from the exact solution

$$u(x, t) = e^{-t} \left(a \cos(\pi x) + b \sin(\pi x) + A \exp(-u_l x) + B \exp(-u_r(1-x)) \right),$$

$$\text{where } a = \frac{(\epsilon\pi^2+1)}{\mu^2\pi^2+(\epsilon\pi^2+1)^2}, \quad b = \frac{\mu\pi}{\mu^2\pi^2+(\epsilon\pi^2+1)^2}, \quad u_{l,r} = \frac{(\mp\mu+\sqrt{\mu^2+4\epsilon})}{2\epsilon}, \quad A = -a \frac{1+\exp(-u_r)}{1-\exp(-(u_l+u_r))}, \quad B = a \frac{1+\exp(-u_l)}{1-\exp(-(u_l+u_r))}.$$

We executed the code for 1000 iterations, and the computed errors at the final time $T = 1$ are reported in Table 5. Figure 16 illustrates the comparison between the exact solution and the VPINN approximation for various parameter values at $T = 1$. The corresponding absolute error distributions are shown in Figure 17. Figure 18 displays the loss versus epoch curves, which represent the convergence behavior during the final iteration of the algorithm. Additionally, Figure 19 provides a surface plot comparison between the exact solution and the VPINN approximation for various values of the perturbation parameter.

Table 5: Loss and Error for Example 5 at the final time $T = 1$.

ϵ, μ	Loss	maximum	Rel-maximum	L_2	Rel- L_2
$10^{-1}, 10^{-2}$	2.11662e-08	9.28079e-05	1.47207e-03	4.98550e-05	1.11424e-03
$10^{-2}, 10^{-3}$	6.82480e-06	1.59839e-03	7.02785e-03	8.08532e-04	4.99766e-03
$10^{-3}, 10^{-4}$	2.49291e-05	5.49714e-03	1.65834e-02	1.62604e-03	7.03748e-03
$10^{-4}, 10^{-5}$	3.25968e-05	2.22948e-02	6.18356e-02	3.18900e-03	1.27222e-02

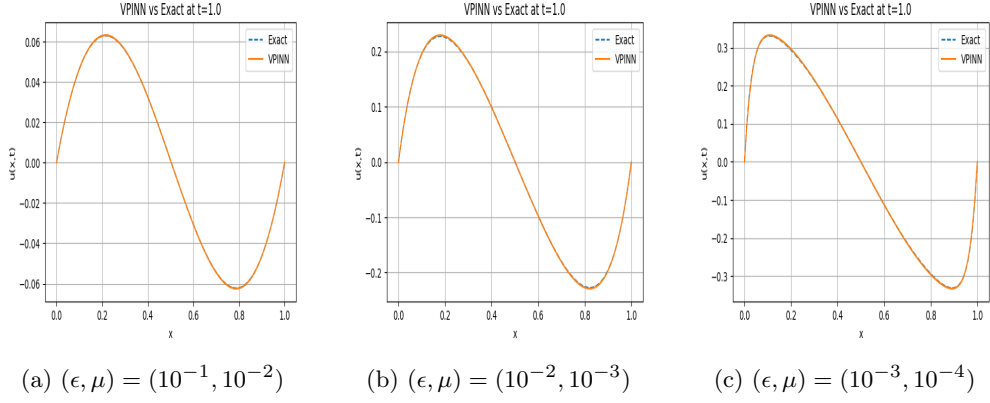


Fig. 16: Comparison between Exact and VPINN solution for Example 5 with different value of perturbation parameter.

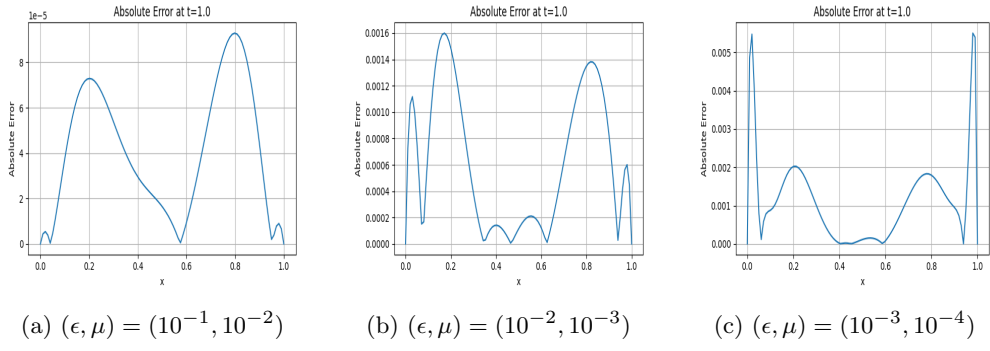


Fig. 17: Error vs x for Example 5 with different value of perturbation parameter.

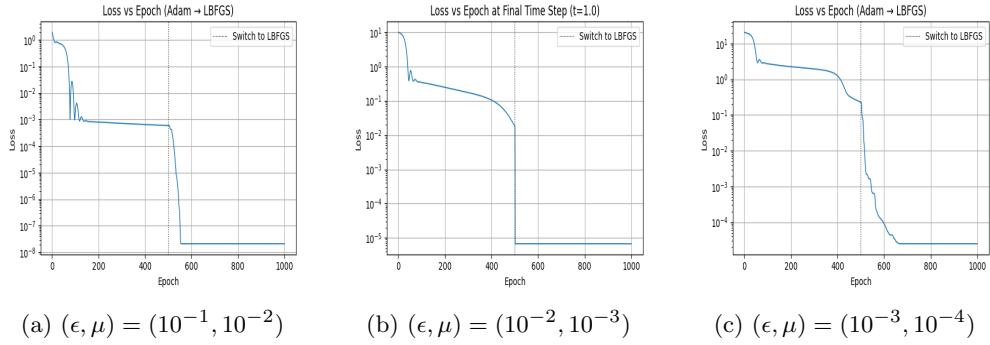
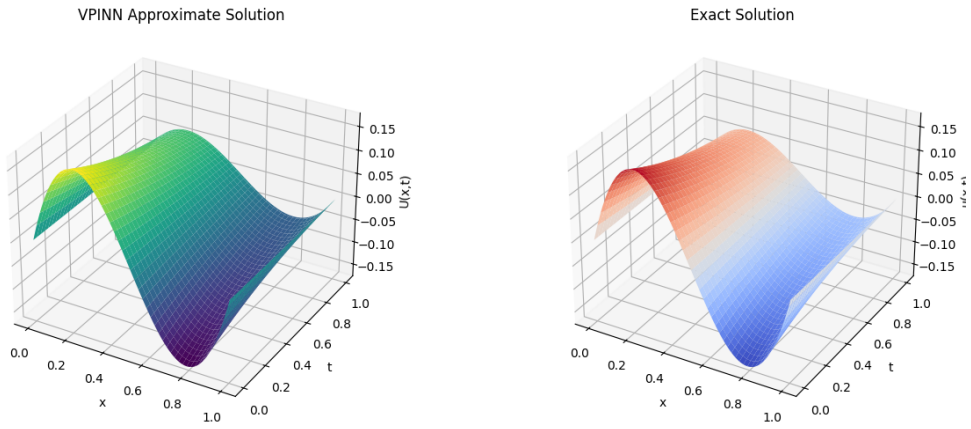
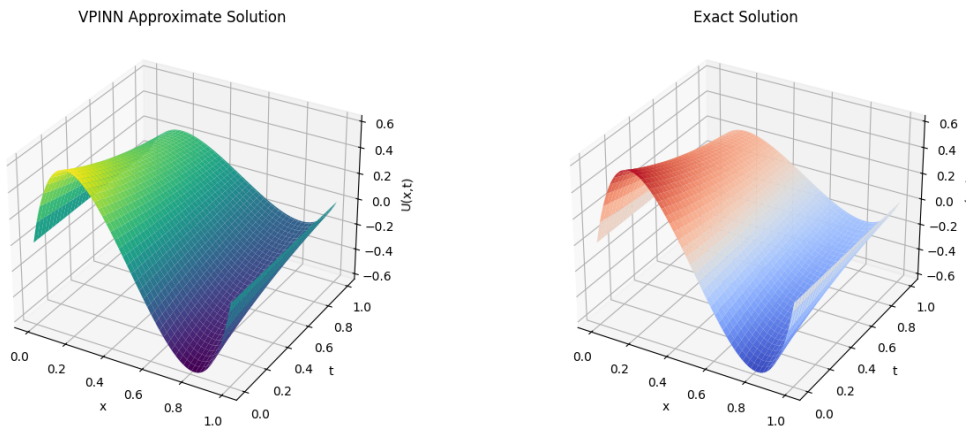


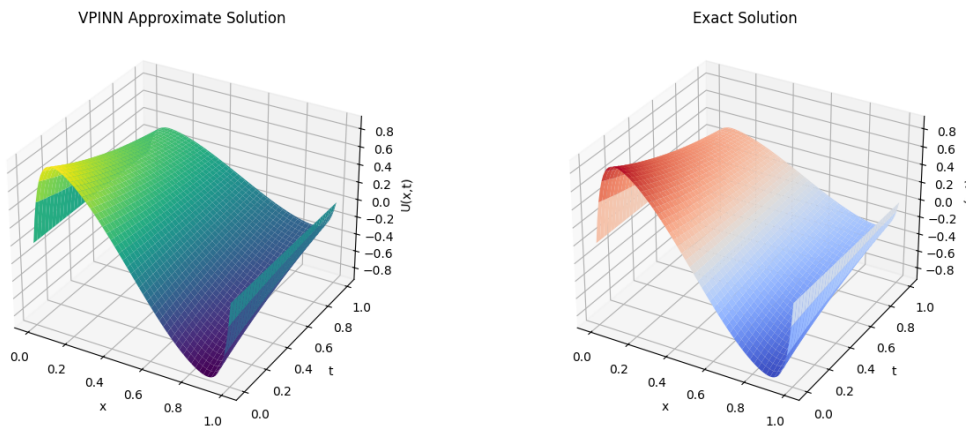
Fig. 18: Loss vs Epoch for Example 5 with different value of perturbation parameter.



(a) $(\epsilon, \mu) = (10^{-1}, 10^{-2})$



(b) $(\epsilon, \mu) = (10^{-2}, 10^{-3})$



(c) $(\epsilon, \mu) = (10^{-3}, 10^{-4})$

Fig. 19: Comparison between exact solution vs approximate solution for Example 5 with perturbation parameter.

4 Conclusion

In this article, we presented a VPINN framework based on the Petrov-Galerkin method for solving SPPs. The solution was approximated using DNNs for the trial space, while the test space consisted of localized hat functions. This setup allowed for effective handling of sharp boundary layers without relying on dense mesh discretizations. For time-dependent problems, we employed the backward Euler scheme for temporal discretization. The training process combined the strengths of both ADAM and L-BFGS optimizers starting with ADAM for faster initial progress and then refining with L-BFGS. Source terms were evaluated through automatic differentiation, enhancing accuracy within the weak formulation. The proposed VPINN method demonstrated strong performance, offering a stable, accurate, and mesh-free solution technique for both steady and time-dependent SPPs.

Funding

The authors received no external funding for this work.

Conflict of Interest

The authors declare that they have no conflicts of interest.

Data Availability

Not applicable.

References

- [1] K. Alhumaizi. Flux-limiting solution techniques for simulation of reaction-diffusion-convection system. *Commun. Nonlinear Sci. Numer. Simul.*, 12(6):953–965, 2007.
- [2] D. N. Arnold. An interior penalty finite element method with discontinuous elements. *SIAM journal on numerical analysis*, 19(4):742–760, 1982.
- [3] D. Avijit and S. Natesan. A novel two-step streamline-diffusion FEM for singularly perturbed 2D parabolic PDEs. *Appl. Numer. Math.*, 172:259–278, 2022.
- [4] P. Boro, A. Raina, and S. Natesan. A parameter-driven physics-informed neural network framework for solving two-parameter singular perturbation problems involving boundary layers, 2025. <https://arxiv.org/abs/2505.01159>
- [5] F. Cao, F. Gao, X. Guo, and D. Yuan. Physics-informed neural networks with parameter asymptotic strategy for learning singularly perturbed convection-dominated problem. *Comput. Math. Appl.*, 150:229–242, 2023.
- [6] G. Capuano and J. J. Rimoli. Smart finite elements: a novel machine learning application. *Comput. Methods Appl. Mech. Engrg.*, 345:363–381, 2019.
- [7] G. Chen, S. Xu, D. Ni, and T. Zeng. Dgnn: A neural pde solver induced by discontinuous galerkin methods, 2025. <https://arxiv.org/abs/2503.10021>
- [8] R. Hartmann and P. Houston. Symmetric interior penalty DG methods for the compressible Navier-Stokes equations. II. Goal-oriented a posteriori error estimation. *Int. J. Numer. Anal. Model.*, 3(2):141–162, 2006.
- [9] J. S. Hesthaven and S. Ubbiali. Non-intrusive reduced order modeling of nonlinear problems using neural networks. *J. Comput. Phys.*, 363:55–78, 2018.
- [10] E. Kharazmi, Z. Zhang, and G. E. Karniadakis. Variational physics-informed neural networks for solving partial differential equations, 2019. <https://arxiv.org/abs/1912.00873>
- [11] E. Kharazmi, Z. Zhang, and G. E. Karniadakis. *hp*-VPINNs: variational physics-informed neural networks with domain decomposition. *Comput. Methods Appl. Mech. Engrg.*, 374:113547, 25, 2021.
- [12] P. V. Kokotović. Applications of singular perturbation techniques to control problems. *SIAM Rev.*, 26(4):501–550, 1984.
- [13] Heinz-Otto Kreiss and Jens Lorenz. *Initial-boundary value problems and the Navier-Stokes equations*, volume 47 of *Classics in Applied Mathematics*. Society for Industrial and Applied Mathematics (SIAM), Philadelphia, PA, 2004. Reprint of the 1989 edition.

- [14] I.E. Lagaris, A. Likas, and D.I. Fotiadis. Artificial neural networks for solving ordinary and partial differential equations. *IEEE Transactions on Neural Networks*, 9(5):987–1000, 1998.
- [15] Ke Li, Kejun Tang, Tianfan Wu, and Qifeng Liao. D3m: A deep domain decomposition method for partial differential equations. *IEEE Access*, 8:5283–5294, 2020.
- [16] J. M. Melenk and C. Xenophontos. Robust exponential convergence of *hp*-FEM in balanced norms for singularly perturbed reaction-diffusion equations. *Calcolo*, 53(1):105–132, 2016.
- [17] B. Moseley, A. Markham, and T. N. Meyer. Finite basis physics-informed neural networks (FBPINNs): a scalable domain decomposition approach for solving differential equations. *Adv. Comput. Math.*, 49(4): 62, 39, 2023.
- [18] A. Raina, S. Badireddi, and S. Natesan. Application of pinn to obtain solution of boundary layer problems arising in fluid dynamics. *Mathematical Foundations of Computing*, 2025. 10.3934/mfc.2025024
- [19] M. Raissi, P. Perdikaris, and G. E. Karniadakis. Physics-informed neural networks: a deep learning framework for solving forward and inverse problems involving nonlinear partial differential equations. *J. Comput. Phys.*, 378:686–707, 2019.
- [20] A. Rap, L. Elliott, D. B. Ingham, D. Lesnic, and X. Wen. The inverse source problem for the variable coefficients convection-diffusion equation. *Inverse Probl. Sci. Eng.*, 15(5):413–440, 2007.
- [21] W. H. Reed and T. R. Hill. Triangular mesh methods for the neutron transport equation. Technical report, Los Alamos Scientific Lab., N. Mex.(USA), 1973.
- [22] B. Rivière. *Discontinuous Galerkin methods for solving elliptic and parabolic equations*, volume 35 of *Frontiers in Applied Mathematics*. Society for Industrial and Applied Mathematics (SIAM), Philadelphia, PA, 2008. Theory and implementation.
- [23] H. G. Roos and M. Schopf. Convergence and stability in balanced norms of finite element methods on Shishkin meshes for reaction-diffusion problems. *ZAMM Z. Angew. Math. Mech.*, 95(6):551–565, 2015.
- [24] H. Schlichting and K. Gersten. *Boundary-layer theory*. Springer-Verlag, Berlin, ninth edition, 2017.
- [25] G. Singh and S. Natesan. Study of the NIPG method for two-parameter singular perturbation problems on several layer adapted grids. *J. Appl. Math. Comput.*, 63(1-2):683–705, 2020.

- [26] G. Singh and S. Natesan. Superconvergence error estimates of discontinuous Galerkin time stepping for singularly perturbed parabolic problems. *Numer. Algorithms*, 90(3):1073–1090, 2022.
- [27] M. K. Singh, G. Singh, and S. Natesan. A unified study on superconvergence analysis of Galerkin FEM for singularly perturbed systems of multiscale nature. *J. Appl. Math. Comput.*, 66(1-2):221–243, 2021.
- [28] J. Sirignano and K. Spiliopoulos. DGM: a deep learning algorithm for solving partial differential equations. *J. Comput. Phys.*, 375:1339–1364, 2018.
- [29] L. Tobiska. Analysis of a new stabilized higher order finite element method for advection-diffusion equations. *Comput. Methods Appl. Mech. Engrg.*, 196(1-3):538–550, 2006.
- [30] S. Yadav and S. Ganesan. Artificial neural network-augmented stabilized finite element method. *J. Comput. Phys.*, 499: 112702, 15, 2024.
- [31] Z. Zhang. Finite element superconvergence on Shishkin mesh for 2-D convection-diffusion problems. *Math. Comp.*, 72(243):1147–1177, 2003.